Supporting Information for:

A contribution to the quantification of crustal shortening and kinematics of deformation across the Western Andes (~20–22°S).

Tania Habel[1], Martine Simoes[1], Robin Lacassin[1], Daniel Carrizo[2,3], German Aguilar[2]

[1] Université Paris Cité, Institut de physique du globe de Paris, CNRS, F-75005 Paris, France
[2] Advanced Mining Technology Center, Facultad de Ciencias Físicas y Matemáticas, Universidad de Chile, Avenida Tupper 2007, Santiago, Chile
[3] now at GeoEkun SpA, Santiago 7500593, Chile

Correspondence to: Martine Simoes (simoes@ipgp.fr)

Contents of this file

Additional Supporting Information (Files uploaded separately)
Caption for Dataset S1

Introduction

This supporting information document is subdivided into three sections:

(1) Various sedimentary and structural details from the Pinchal zone.

A sedimentary description of the units encountered in the Pinchal zone, further illustrating section 4.1 and Figure 3 is first provided through field photographs (Figures S1–S12) and their position is reported on the corresponding structural map (Figure S14).
Structural details on penetrative deformation are given on Figure S13 and located on the structural map of Figure S14.
Non-interpreted field photographs of Figures 6 and 7 are also provided for reference (Figures S15 and S16).

(2) Landscape views and structural details from the Quebrada Blanca area.

Structural details on the eastern anticline are provided in Figure S17. Figure S18 provides an interpreted and non-interpreted view of the western small-scale anticlines.

(3) Additional information on trishear modeling.

Here, we present further details on the trishear modeling method and on our results (Text S1), complementary to sections 3.4, 6.3 and 6.4 in the main text. This text is accompanied by figures illustrating six key stages of our preferred trishear model for Quebrada Tambillo (Figure S19) and Quebrada Blanca (Figure S20). A table showing the range of tested parameters for modeling (Table S1) is provided. Parameters of our preferred models are indicated in Table S2 and S3 for the sections of Quebrada Tambillo and Quebrada Blanca, respectively.

Additional dataset

In addition to this document, we provide geo-referenced information for our field logistics (field_Habel_etal__SE_2022.kmz). This dataset allows for visualizing on Google Earth the off-road track we used to reach the extremely remote Pinchal area, the location of our Pinchal base-camp, and the GPS positions of field photographs for both study sites. In hyper-arid environments such as here, tracks may be preserved for several years, in between two rare rain episodes. We therefore recall that the off-road track and base-camp indicated here were those of March 2018 and January 2019, and cannot guarantee their state and usability after that period.

All the photographs (presented in the supporting information and in the main text) were taken by us during our field missions in March 2018 and January 2019.

(1) Pinchal area

Figure S1. Migmatitic gneisses, a common metamorphic facies found in the Paleozoic basement rocks to the east of the Pinchal area. Hiking stick given for scale. Location #S1 on Figures 3 and S14.

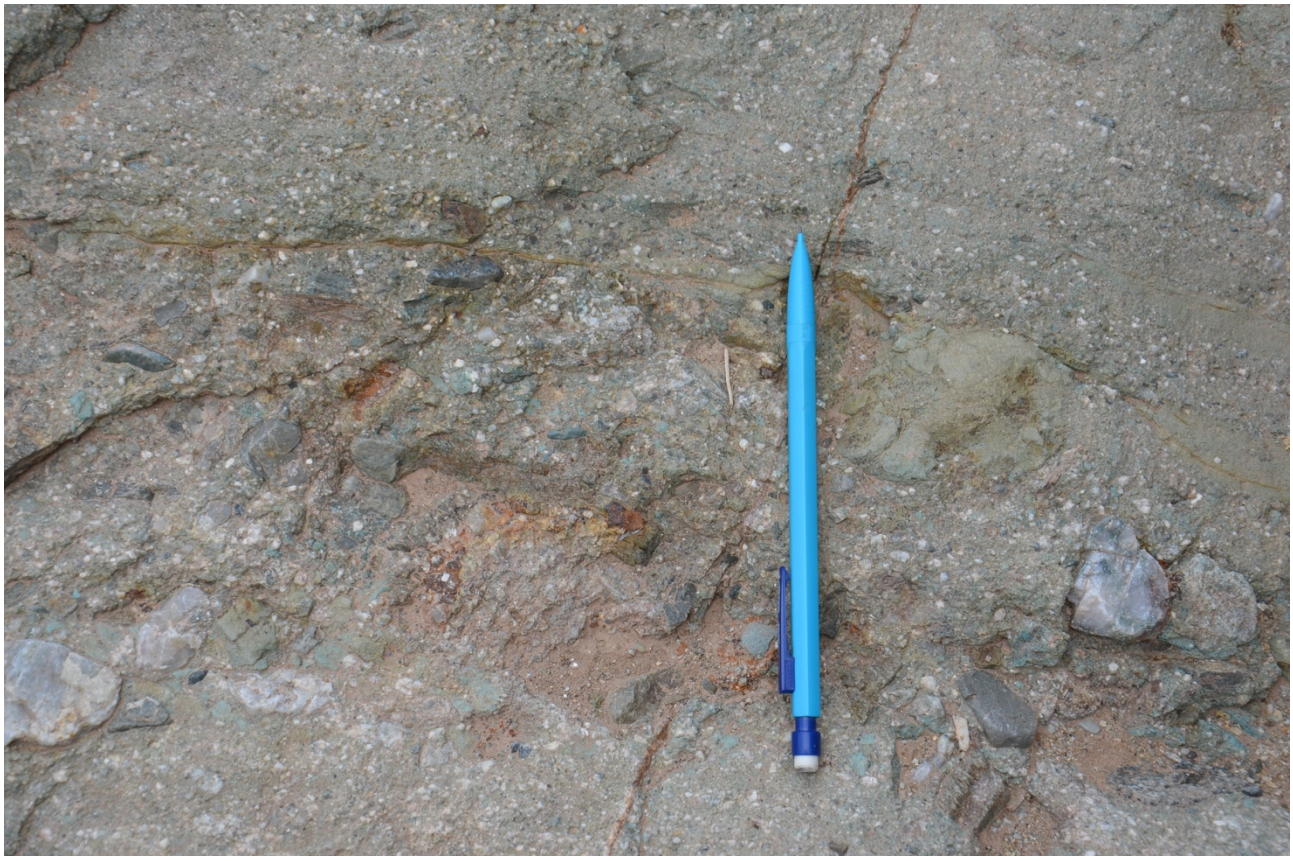

Figure S2. Volcano-detrital conglomerates, here of greenish color, belonging to the older continental Mesozoic series, with millimetric to centimetric clasts. Location #S2 on Figures 3, 5a, and S14.

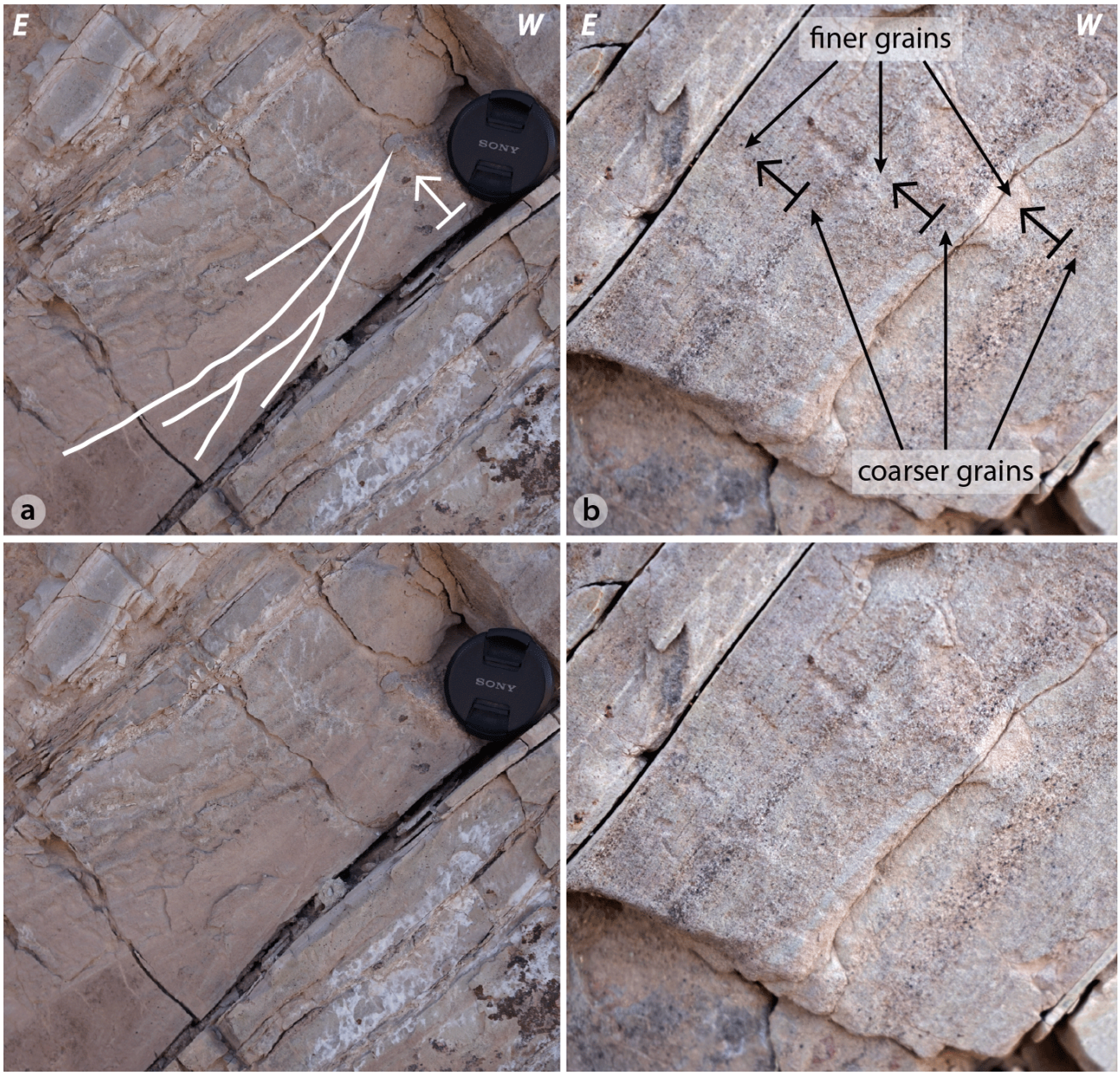

Figure S3. Detrital layers within the Mesozoic units, characterized by (a) tangential beds, indicative of normal polarity with top-to-the-east; (b) grain-size grading (finer at the top, coarser at the base of the layer) indicating top-to-the-east bedding polarity. Note also the erosive base contrasting with the sharp top of the layer. Top: interpreted field pictures; bottom: non-interpreted pictures. Location #S3 on Figures 3 and S14.

Figure S4. Dark green detrital pelites (lutites). This unit resembles sediments given a Triassic age (Aguilef et al., 2019) immediately north of the Pinchal area. Note the strong deformation as these lutites are located next to the Pinchal Thrust. Location #S4 on Figures 3, 5a, and S14.

Figure S5. Silex nodules at the base of the calcareous crest (blue pencil for scale). Location #S5 on Figures 3, 5a, and S14.

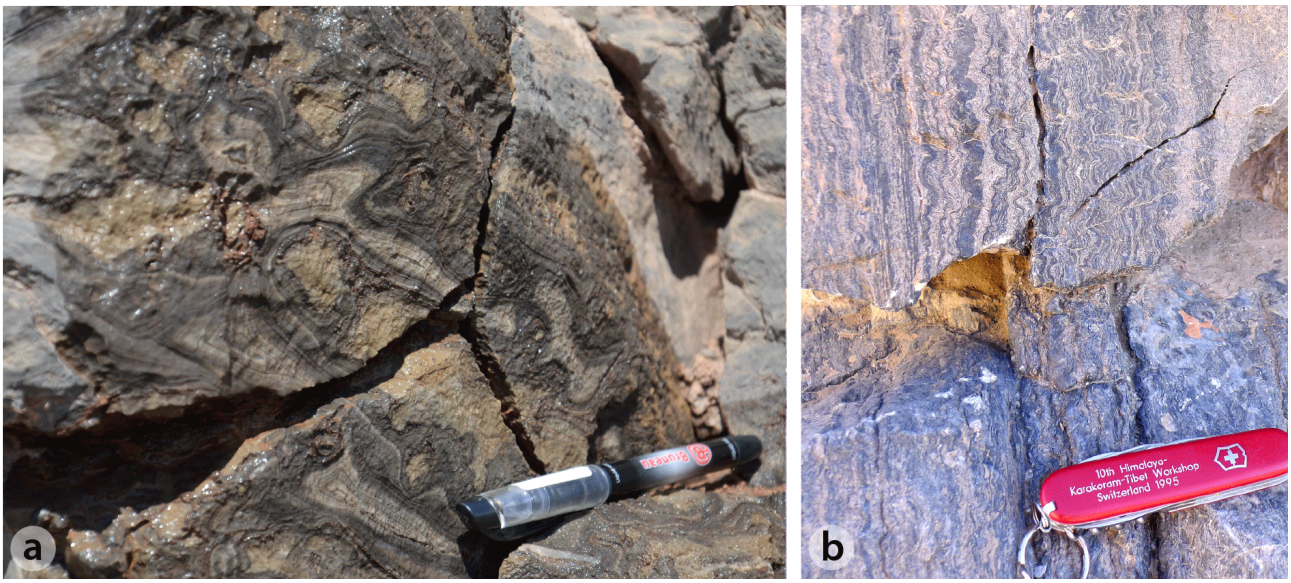

Figure S6. Stromatolite fossils from the Mesozoic (marine) series, located within (a) the western normal synclinal fold limb; and (b) the eastern inverted synclinal fold limb. Location #S6a and S6b, respectively, on Figures 3 and S14.

Figure S7. Bivalve fossils from the Mesozoic (marine) series, located within the western normal synclinal fold limb. Location #S7 on Figures 3 and S14.

Figure S8. Fine limestone layers within the Mesozoic (marine) series, characterized by a rose-beige color and an alternance of thin-bedded (cm–dm), regular beds. Location #S8 on Figures 3, 5a, and S14.

Figure S9. Nodule bearing marls from the Mesozoic (marine) series. The nodules vary in size from centimeters to few meters, as in the case of the large ones illustrated in this field photo. Location #S9 on Figures 3, 5a, and S14.

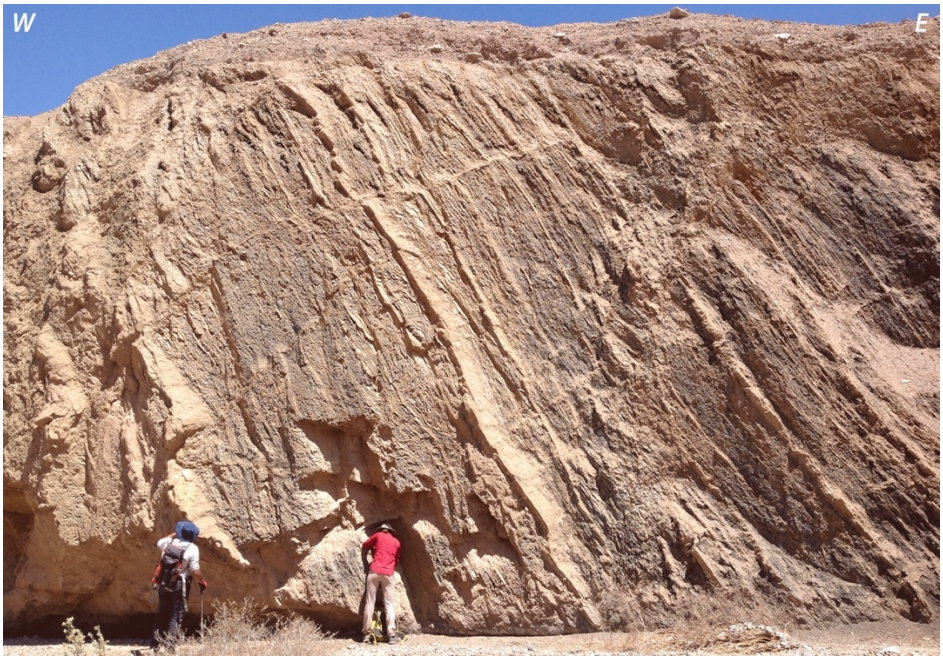

Figure S10. Thin-layered limestone series within marls. Location #S10 on Figures 3, 5b, and S14.

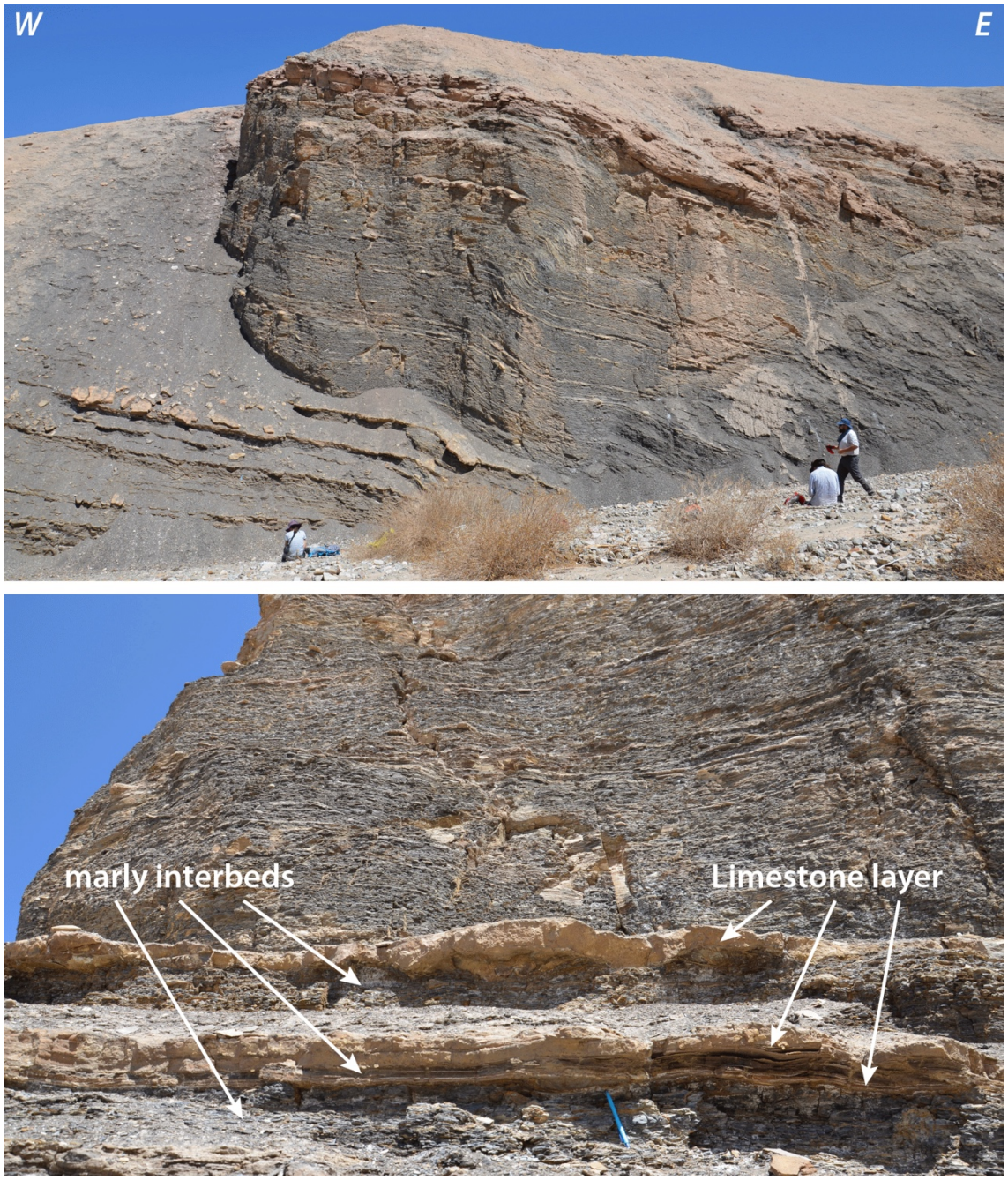

Figure S11. Flysch formation characterized by beige, resistant limestone or sandstone beds of millimetric to decimetric thickness, within dark-grey, more friable, marls. Top: landscape view; bottom: detailed outcrop view (blue pencil for scale). Location #S11 on Figures 3, 5b, and S14.

Figure S12. Red arenites at the base of the Cenozoic series bearing detrital and volcanic clasts of millimetric to pluri-centimetric size. Location #S12 on Figures 3 and S14.

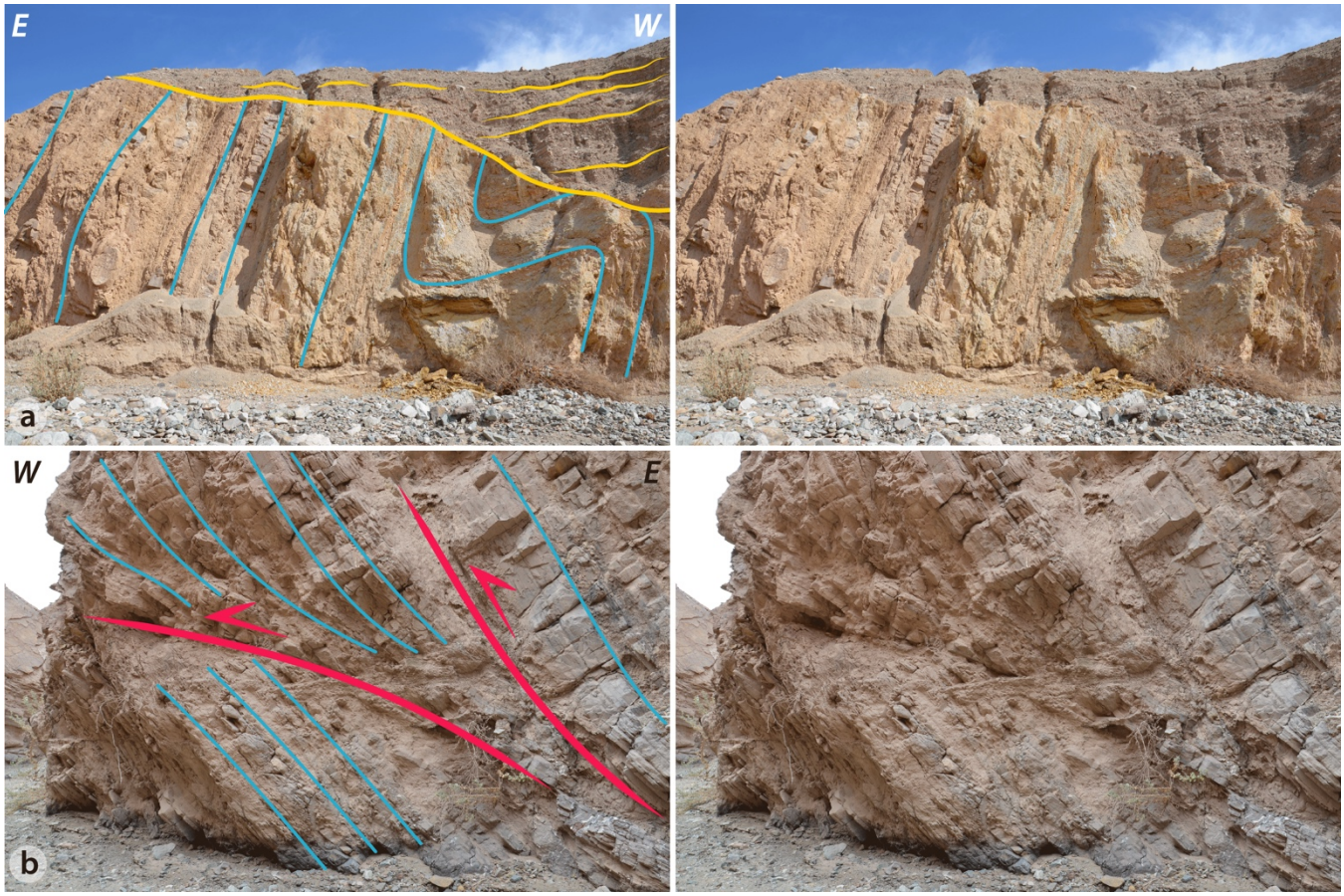

Figure S13. Field pictures of small-scale structural features characteristic of the deformation within the Pinchal zone (Locations #S13 on Figure S14). Left: interpreted picture; right: non-interpreted picture.
(a) Example of a small-scale fold within the marine Mesozoic units (blue line) in Quebrada Tania, within the inverted limb of the mapped syncline, nearby the fold axis. Note also the erosional surface (yellow) forming the unconformable contact between the Cenozoic deposits over the deformed Mesozoic.
(c) Small-scale thrusts (steep red line to the right) and décollements (flat red line to the left) observed within the marine Mesozoic strata (blue) of the inverted synclinal limb along Quebrada Tania. The limestone-dominated cm–dm beds are characteristic of the lower part of the marine Mesozoic units.

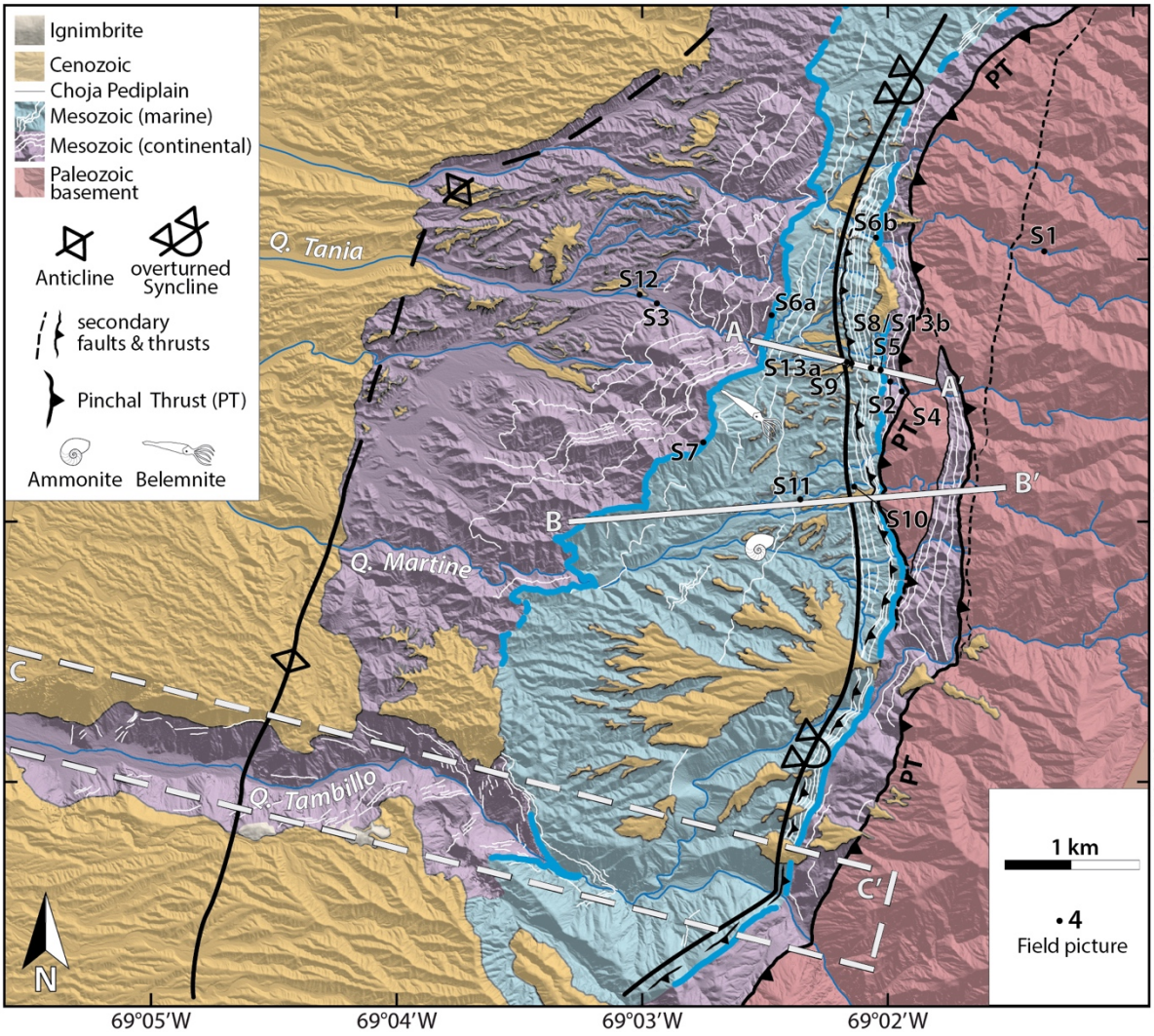

Figure S14. Structural map of the Pinchal area, similar to Figure 4 in main text but here with locations of supplementary field references (S1–S13). Field photographs are located and numbered according to the figures where shown. Location of this map is the same as that of Figure 4, reported on Figure 1. White thin lines highlight Mesozoic layers mappable on satellite images. Thick blue line depicts the calcareous crest, which is used as a marker bed (Figure 2). A–A' and B–B' locate the cross-sections of Quebrada Tania and Quebrada Martine, respectively (Figures 5a-b). In the case of the Quebrada Tambillo cross-section, a topographic swath profile was used along C–C' (dashed box). The fold axes are relatively well defined for the synclinal fold, but less well constrained for the anticlinal fold because only observable along Quebrada Tambillo. Background hillshaded DEM produced from tri-stereo Pléiades imagery. Q: Quebrada (Spanish word for "canyon").

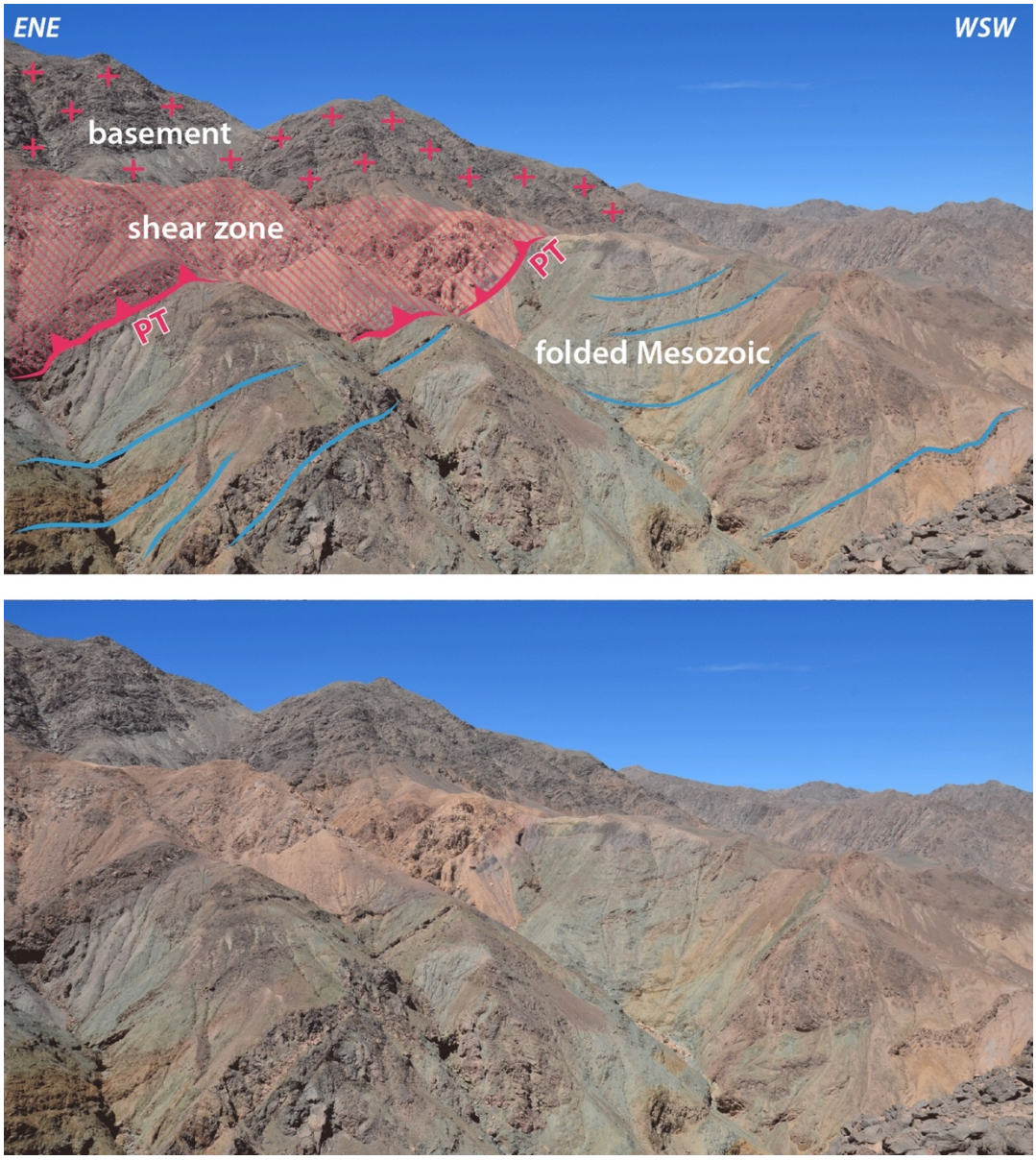

Figure S15. Field view of the Pinchal Thrust (PT), overthrusting the dark-grayish Paleozoic basement over the greenish folded Mesozoic units. Reddish rocks on the hanging wall to the East-Northeast correspond to the thrust shear zone (hatched area in picture). Same as Figure 6a (Top), but with non- interpreted field picture (bottom). Location #6a on Figure 4.

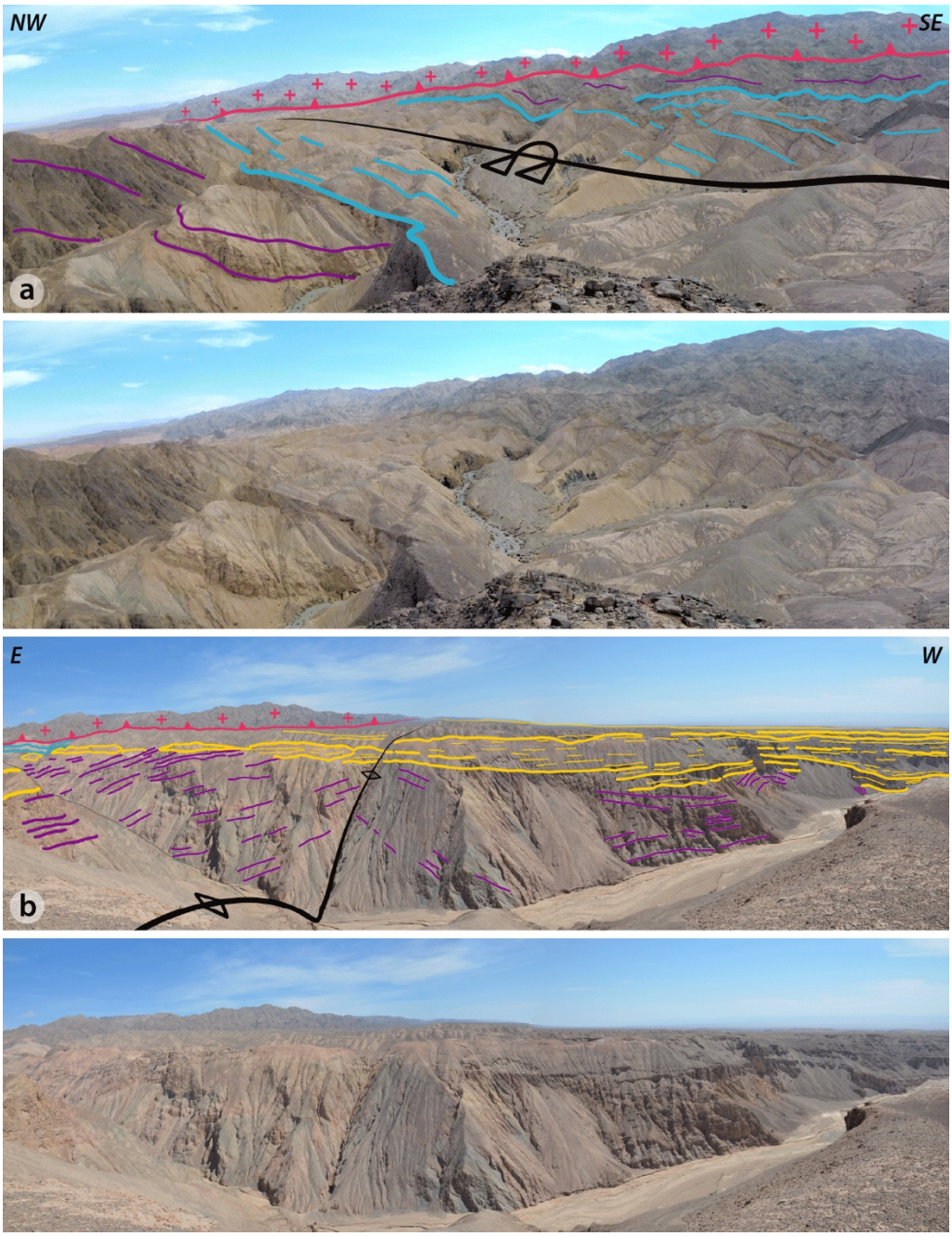

Figure S16. Field pictures of the two major folds within the Pinchal zone, as in Figure 7 in main text. Location #7a and 7b in Figure 4. (a) Panoramic view over the north-eastern part of the Pinchal area. (b) Panoramic view along Quebrada Tambillo, in the southern part of the Pinchal area. Top: interpreted picture; bottom: non-interpreted picture, for (a) and (b) respectively. For complete figure descriptions see main text.

(2) Quebrada Blanca

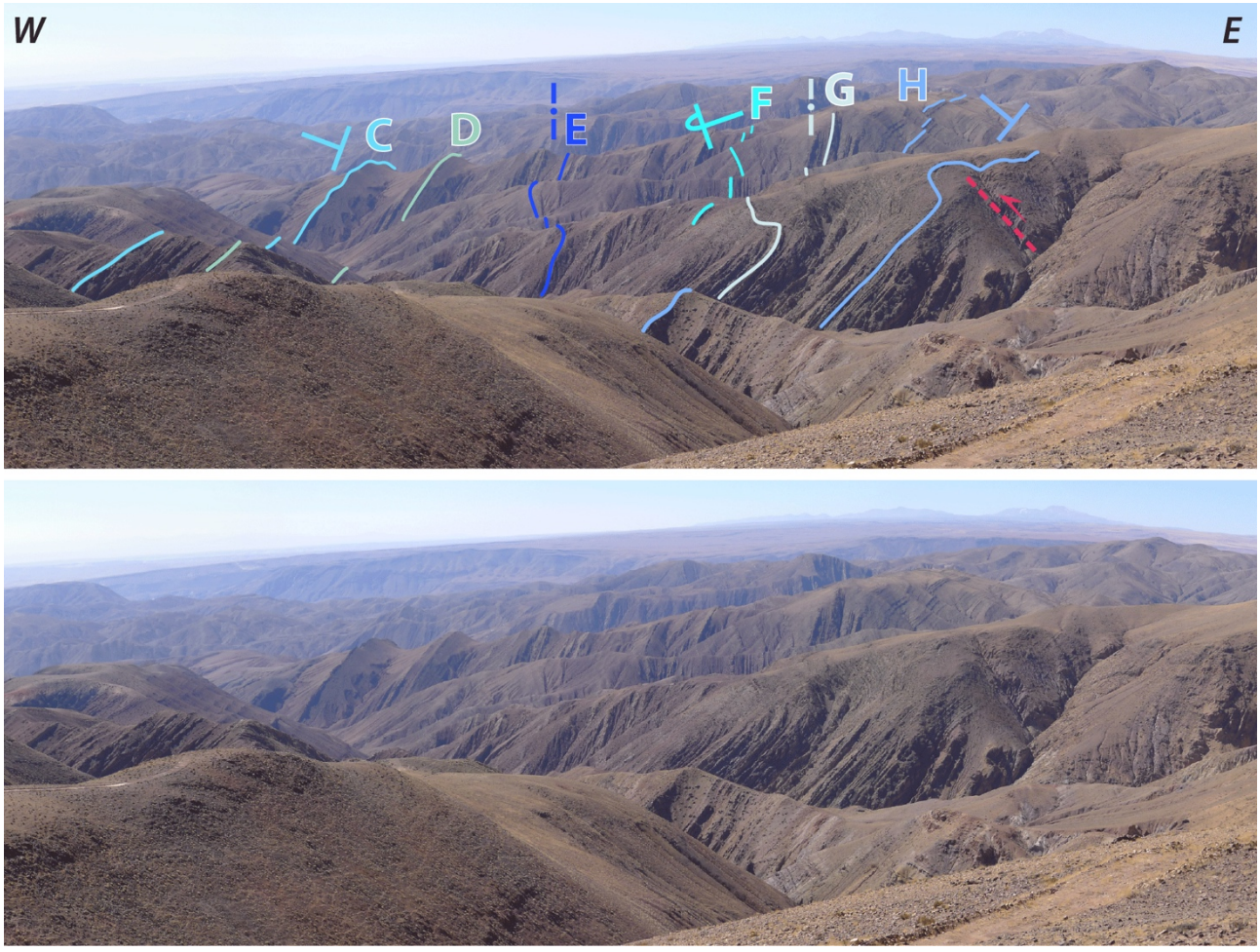

Figure S17. Landscape view on the western limb of the eastern large-scale anticline in the Quebrada Blanca area (Location on Figures 8 and 9). Here, steeply inclined Mesozoic horizons are very well discernible in the landscape. Bedding traces C, D, E, F, G and H underlined here are also georeferenced on the structural map (Figure 8) from mapping on satellite imagery. Note the thrust-affected small-scale fold (red dashed line) emphasizing the west-vergence of tectonic structures. The non-interpreted picture is also provided for reference.

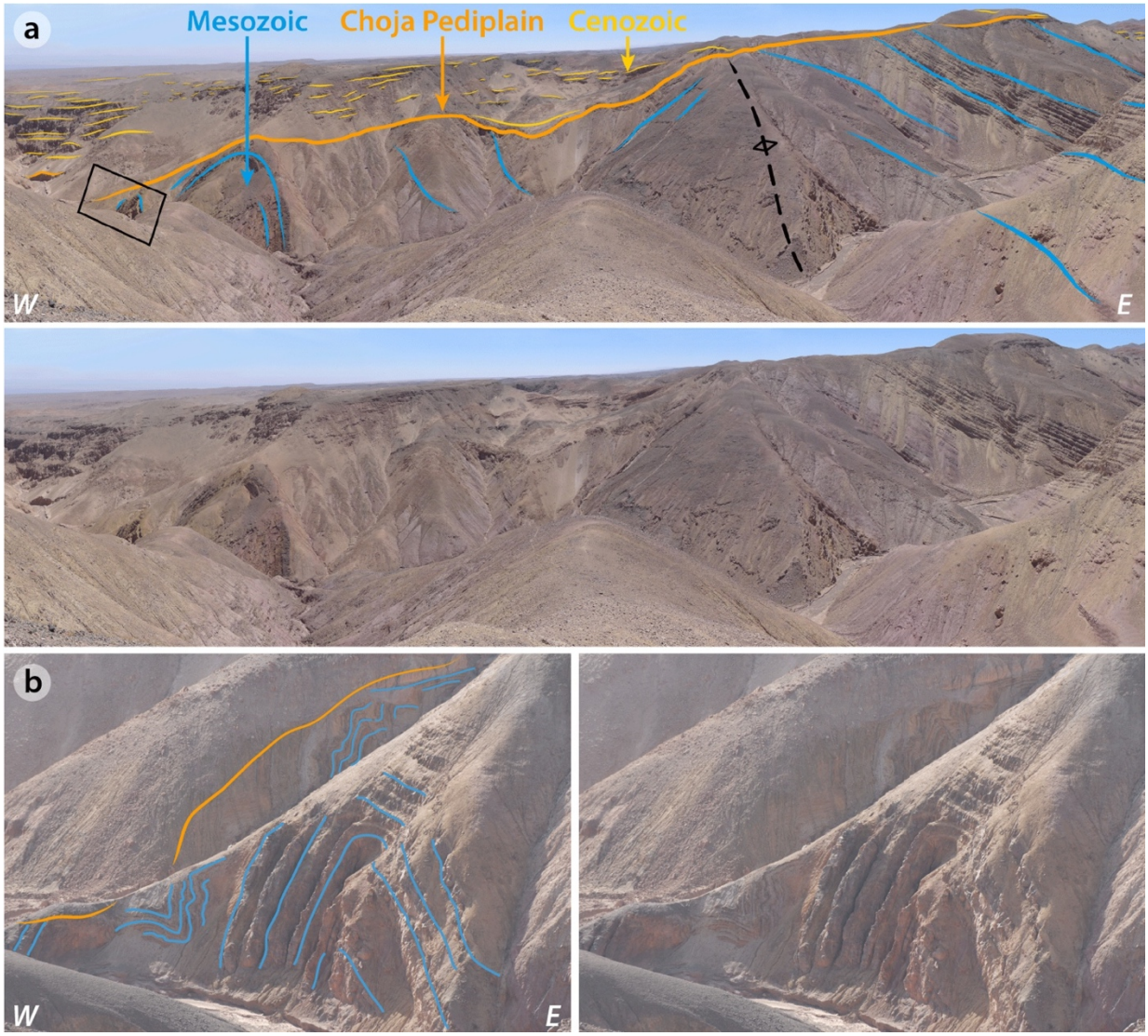

Figure S18. Field picture of the western limb of the western anticline in the Quebrada Blanca area. Same as Figure 10 in main text. Location #10 in Figure 8.
(a) Series of folds with westward decreasing amplitude and wavelength (hundreds to tens of meters) observed at the front of the western anticline. Top: interpreted picture; bottom: non-interpreted picture.
(b) Detailed view of the westernmost outcropping small-scale anticlines, located on (a) by the black box. Left: interpreted picture; right: non-interpreted picture.

(3) Trishear modeling

Text S1. Additional information on trishear modeling (method and results)

As briefly resumed in sections 3.4, 6.2 and 6.3, we used the trishear folding approach (e.g. Allmendinger, 1998; Erslev, 1991) to better constrain the amount of shortening across our study areas, building after our preferred structural interpretation of field data (Figure 11). We further detail the trishear method and results here.

Method

We assume fault-propagation folding to be the dominant mode of deformation in the studied fold-and-thrust-belt, and in particular in the case of the western anticlines of the cross-sections along Quebrada Tambillo (Pinchal area) and Quebrada Blanca. This relates to the fact that faults remain blind and are associated with dishamornic folding at their probable tip (ie small-scale folds at the front of western anticlines).

We use the code FaultFold Forward version 6 (freely available from http://www.geo.cornell.edu/geology/faculty/RWA/programs/faultfoldforward.html, Allmendinger 1998) that models the distributed deformation in triangular zones at the tip of propagating faults. The formalism relies on the following parameters: the coordinates of the fault tip, the angle of the propagating fault ramp, the slip on the fault, the propagation-to-slip-ratio (P/S) of the fault, the trishear angle (i.e. the angle of the triangular zone at the tip of the fault where distributed deformation occurs), and the inclined shear angle (either parallel or similar folding) controlling the backlimb kinematics. We assume here the case of linear symmetric trishear to keep models as simple as possible, meaning that folding of the backlimb occurs parallel to the fault. We tested non-linear trishear but these trials lead to unsatisfying results when compared to our cross-sections.
For the initial conditions of the models, we assume slightly sub-horizontal layers, with a slight eastward tilt (3°E at Quebrada Tambillo, 2°E at Quebrada Blanca) as expected in the initial Andean basin. The final geometry of the fold and sedimentary cover, the fault ramp angles and bends are constrained to fit our geological cross-sections.
By adding sedimentary layers step by step during progressing deformation, we model syntectonic deposition of the Cenozoic series and reproduce the angular unconformity of the Cenozoic over Mesozoic units. The syntectonic deposits are also assumed to be initially slightly sub- horizontal, here with a slight westward tilt (3°W at Quebrada Tambillo, 6°W at Quebrada Blanca), following the approximate angle of the present-day average topography in the corresponding study areas. In fact, the basal Choja Pediplain may be comparable to the first order to the present-day average rising topography; subsequent deposition along the western mountain flank had most certainly a slight westward tilt as observed today within the eastern Atacama Bench (Figure 1). We tested the addition of horizontal syn-tectonic Cenozoic layers, but the modeled fold-forms were much less consistent with our field and map observations. We tested different dipping angles (between 1–7°W) and chose the values that allowed us to best reproduce our data.

The trishear modeling confirms the necessity of a fault ramp propagating from a deep décollement towards the surface to fit the observed folds, as classically observed in fold-and-thrust belts. We simplify the fault geometry into a few fault segments: 4 segments for Quebrada Tambillo, and 3 segments for Quebrada Blanca (Figures 11, S19 and S20). Segment 1 corresponds to the flat deep detachment which is parallel to the inferred initial Mesozoic bedding. The second fault segment ramps up from this décollement with an eastward dipping angle of 24°E for Quebrada Tambillo, 40.6°E for Quebrada Blanca. These geometries are needed to fit the dip angles observed in the hanging wall of the faults (i.e. within the backlimb of the modeled folds). A shallow flat detachment is needed at both study sites to reproduce the large-scale tilt of the Cenozoic cover and the geometry of fold forelimbs. For Quebrada Tambillo, an 11.3° eastward-dipping fourth segment is necessary to best fit the surface observations in the western part of the cross-section.
Neither the trishear angle, nor the P/S ratio are deductible from geological observations (Allmendinger & Shaw, 2000), while their effect on folding is crucial as pointed out by various studies (e.g. Hardy & Ford, 1997; Allmendinger, 1998;

Zehnder & Allmendinger, 2000). With the aim to satisfactorily reproduce the geometry of the folded Mesozoic units and the tilt of the Cenozoic strata cover (Figures 5 and 9), we tested 65-100 combinations of parameters, in the range of values considered as reasonable in the literature (e.g. Allmendinger, 1998; Allmendinger & Shaw, 2000; Cristallini & Allmendinger, 2002; Hardy & Ford, 1997; Zehnder & Allmendinger, 2000) and regarding our geological constraints. By trial and error, we thus establish a set of preferred parameters for Quebrada Tambillo and Quebrada Blanca respectively, indicated in Tables S1 to S3. The effect of the various parameters on the fold geometries has been separately and manually tested so as to converge progressively to a viable and reasonable solution. We recognize here that these may not be unique but only represent possible geologically viable solutions.

Results

The final stages (i.e. present-day deformation pattern) of our preferred models are represented in Figure 11 (main text), together with the corresponding structural cross-sections. The cumulative shortening, as constrained by the trishear modeling, in agreement with our geological cross-sections, is of 3.1 km for Quebrada Tambillo, and of 6.6 km for Quebrada Blanca (Figure 11). We recall here that these values account for folding and fault slip, but only for the westernmost anticlines and the two study sites.

Figures S19 and S20 illustrate the various stages of folding and fault propagation of our models, and complement the findings and discussion of sections 6.3 and 6.4 in the main text. Some chronological constraints can be added to these various stages using geological observations, from the initial conditions prior to folding (~68 Ma), the first Cenozoic syn-tectonic deposits (~29 Ma) and to the present-day situation (0 Ma). Considering this, we find that most folding occurred prior to the first Cenozoic deposits of the Altos de Pica Formation at ~29 Ma (stage 3 on Figures S19-S20): before ~29 Ma, 2.6 km (out of the total 3.1 km) and 6.2 km (out of the total 6.6 km) of shortening had been completed for Quebrada Tambillo and for Quebrada Blanca, respectively. After ~29 Ma, the amount of additional shortening is only of 0.5 km and 0.4 km for Quebrada Tambillo and Quebrada Blanca, respectively, and corresponds to less than 20% (16% and 6%, respectively) of the total shortening, even though the duration of both time spans (~68–29 Ma and ~29–0 Ma periods) is of the same order. These findings are further represented on the graph of Figure 11d in the main text.

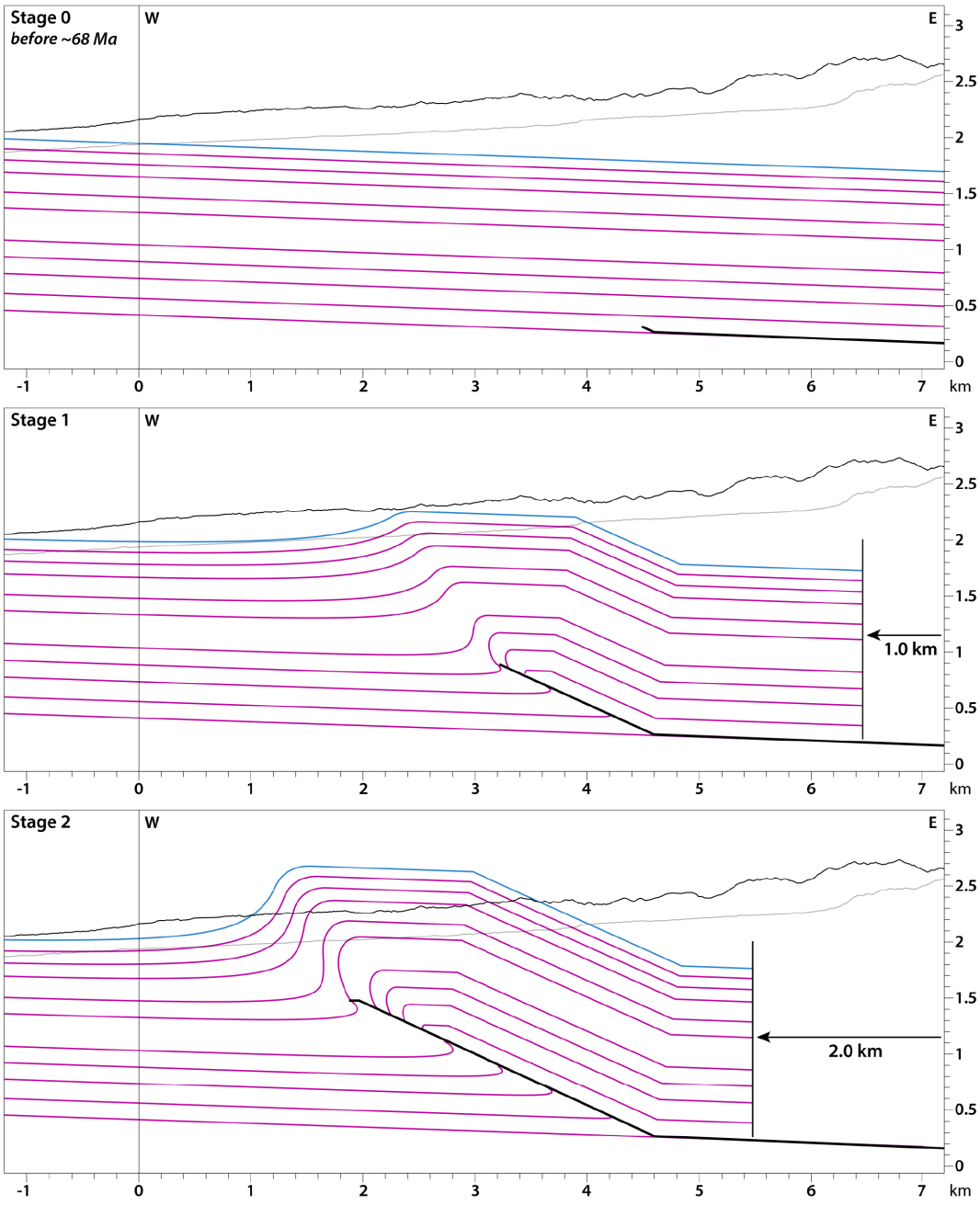

Figure S19. (Following next page)

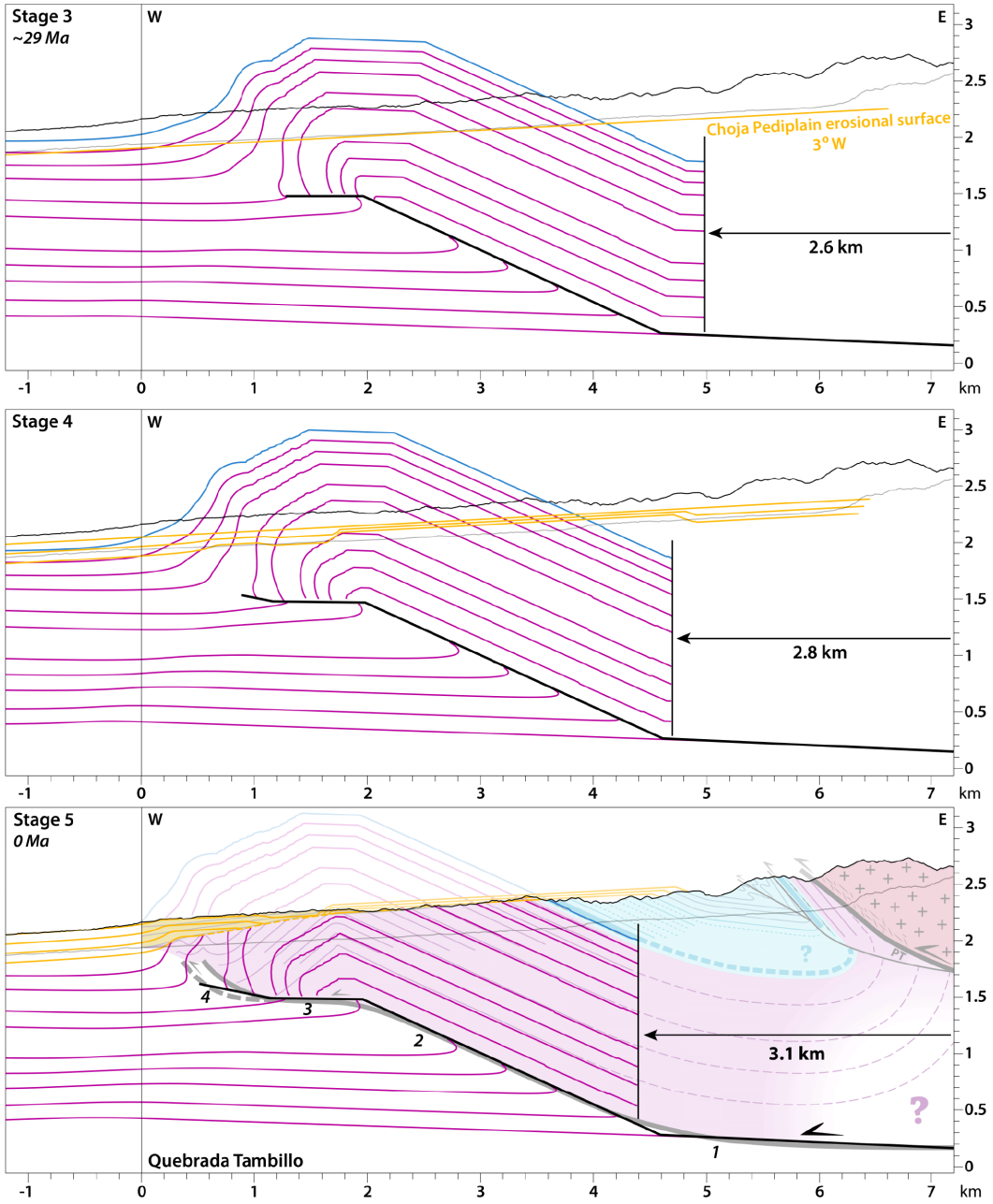

Figure S19. Outcomes from trishear modeling performed with FaultFold Forward v.6 (Allmendinger, 1998) in the case of the Quebrada Tambillo section, with chronological constraints provided from geological observations and data (see section 6.1 in main text). The black horizontal arrows underline the cumulated shortening at each stage. The final stage (present-day situation) is overlapped with our structural cross-section. Model parameters are provided in Table S2. In final stage, fault segments are numbered as in Table S1.

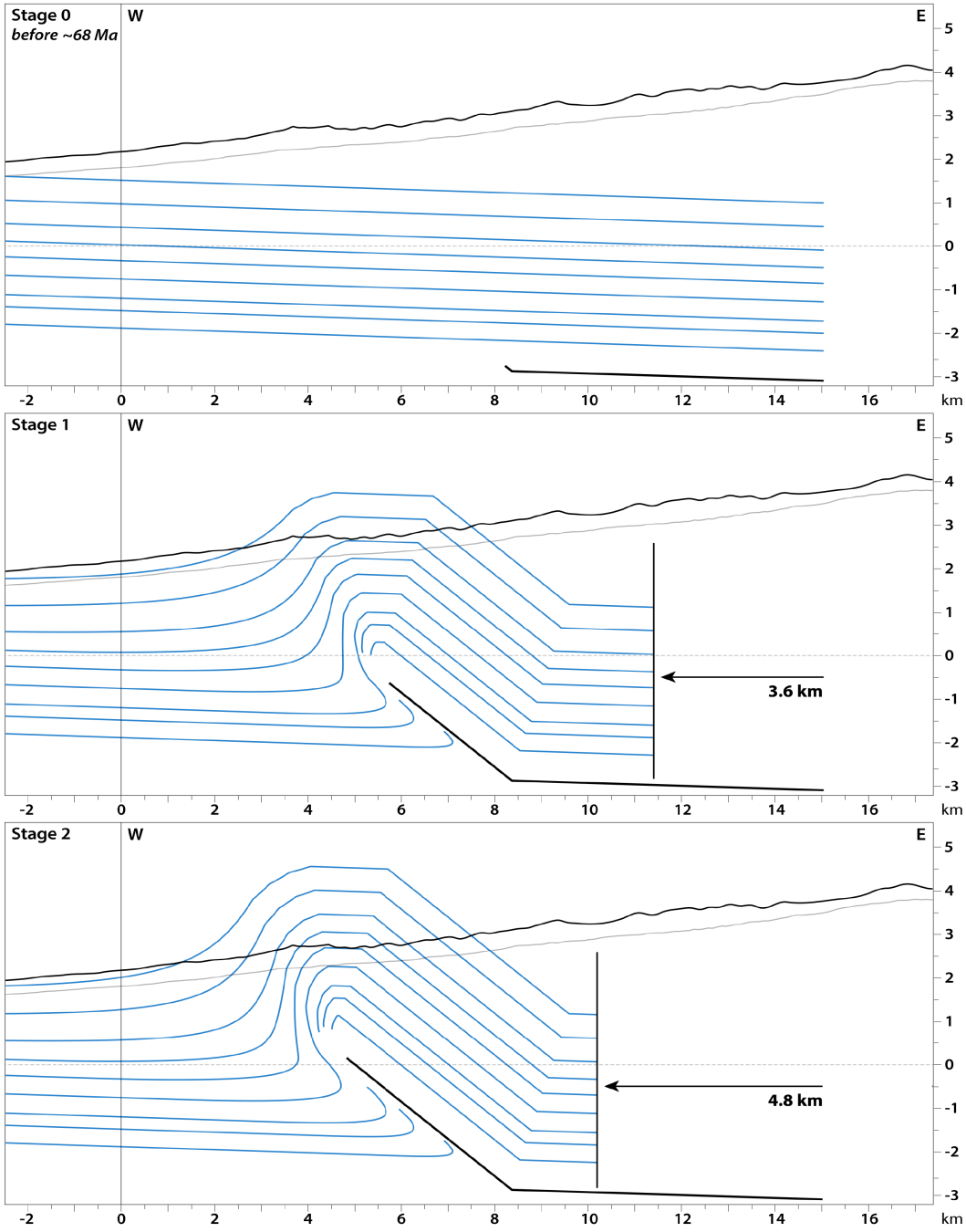

Figure S20. (Following next page)

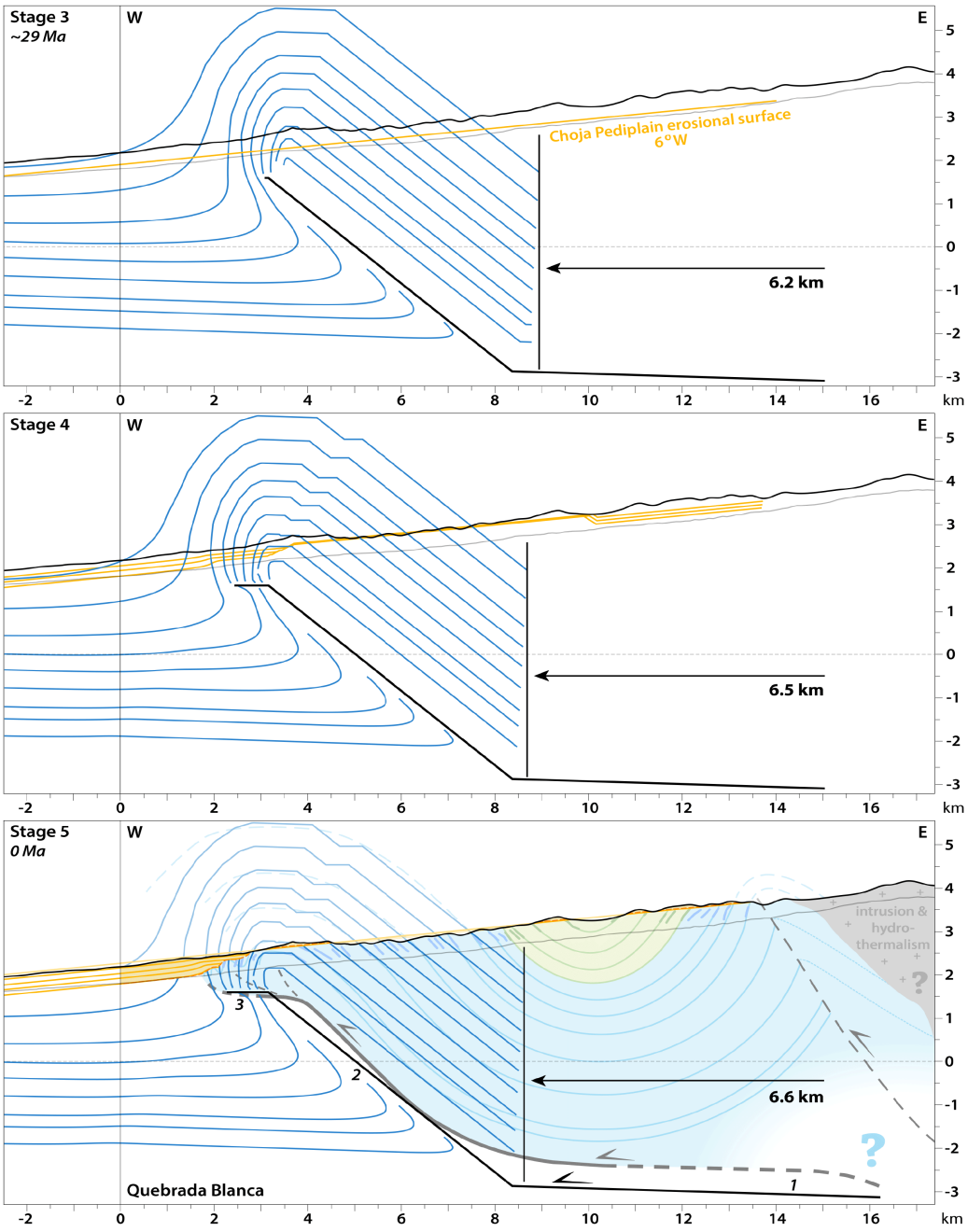

Figure S20. Outcomes from trishear modeling performed with FaultFold Forward v.6 (Allmendinger, 1998) in the case of the Quebrada Blanca section, with chronological constraints provided from geological observations and data (see section 6.1 in main text). The black horizontal arrows underline the cumulated shortening at each stage. The final stage (present-day situation) is overlapped with our structural cross-section. Model parameters are provided in Table S3. In final stage, fault segments are numbered as in Table S1.

	Fault angle	Trishear angle	P/S	Inclined shear angle	Initial bedding dip
Quebrada Tambillo	Segment 1: 0–4°E Segment 2: 20–30°E Segment 3: 0–10°E Segment 4: 5–20°E	50–110°	0.8–3.0	Parallel and similar folding tested	Mesozoic: 0–5°E Cenozoic: 0–4°W
Quebrada Blanca	Segment 1: 0–4°E Segment 2: 30–40°E Segment 3: 0–10°E	50–120°	0.7–3.0	Parallel and similar folding tested	Mesozoic: 0–4°E Cenozoic: 0–7°W

Table S1. Range of tested parameters for the trishear modeling performed with FaultFold Forward v.6 (Allmendinger, 1998). Trial and error forward modeling lead to ~65 tested models for Quebrada Tambillo and ~100 models for Quebrada Blanca. Best results came out with a fault-ramp composed of 4 segments for Quebrada Tambillo, and 3 segments for Quebrada Blanca; segments are here numbered from the deepest to the shallowest. Fault position (tips and bends) and slip on the fault are derived from our geological cross-sections. Initial layer dip angles are chosen in view of the current topography in a range of reasonable initial geometries, which allow to correctly reproduce the sections. The trishear angle controls the size of the deformed area, the P/S (propagation/slip) ratio controls the degree of folding accommodated in the trishear zone. Values for both parameters were tested based on values described as common in the literature. Concerning the inclined shear angle, best fit is obtained with parallel folding for all stages. The inclined shear angle controls the shape of the fold backlimb (Cristallini & Allmendinger, 2002).

Stage	Fault angle	Trishear angle	P/S	Slip (km)	Initial bedding dip
0	3°E	60°	1.4	0	Mesozoic: 3°E
1	24.0°E	60°	1.4	1.0	
2	0°	60°	1.2	2.0	
3	0°	60°	1.2	2.5	
4	11.3°E	90°	1.2	2.6	Cenozoic: 3°W
5	11.3°E	90°	1.2	3.1	

Table S2. Best-fit parameters for the trishear modeling performed with FaultFold Forward v.6 (Allmendinger, 1998) at Quebrada Tambillo. Model results are illustrated on Figure S19.

Stage	Fault angle	Trishear angle	P/S	Slip (km)	Initial bedding dip
0	2°E	50°	0.9	0	Mesozoic: 2°E
1	40.6°E	70°	0.9	3.6	
2	40.6°E	80°	1.0	4.8	
3	0°	90°	0.9	6.2	Cenozoic: 6°W
4	0°	90°	0.9	6.5	
5	0°	90°	0.9	6.6	

Table S3. Best-fit parameters for the trishear modeling performed with FaultFold Forward v.6 (Allmendinger, 1998) at Quebrada Blanca. Model results are illustrated on Figure S20.

Additional Supporting Information (Files uploaded separately)

Data Set S1.

Georeferenced dataset (field_Habel_etal_SE_2022.kmz) for visualization (e.g. on Google Earth) of strategic points during our field missions (in 2018 and 2019). Data points are organized in self-explaining folders:
The folders "major roads" and "dirt tracks" contain lines showing the main paths we followed. Pink, red and orange lines are practicable by (4W drive) cars. White lines are practicable by foot only. Pay attention that we followed the "dirt tracks" for the last time in January 2019. In the case of subsequent rain, even moderate, part of the tracks may have become impracticable by car since then.
The folder "guiding points" comprises strategic (turning-) points on the road, towns and the position of our base-camp in the Pinchal area. Please leave the base-camp always clean and tidy, in the same way as you wish to find it. There, we enjoyed the moon and the stars while cooking excellent French- German-Chilean dishes.
The folder "GPS positions photos" includes two sub-folders for the two investigated areas with the locations of the field photographs equivalent to those depicted on the structural schemes (Figures 4, 8 and S14). Color and symbol of the point-markers give additional information: Paddle symbol stands for view points, pushpin symbol for pictures illustrating stratigraphic and sedimentary observations. Red for Paleozoic basement, blue for Mesozoic units, yellow for Cenozoic deposits. The extent of structural maps of Figures 4 (Pinchal area) and 8 (Quebrada Blanca area) are also reported.

References

Aguilef, S., Franco, C., Tomlinson, A., Blanco, N., Alvarez, J., Montecino, D., et al. (2019). Geología del área Quehuita-Chela, Regiones de Tarapacá y Antofagasta. Santiago, Chile: SERNAGEOMIN.

Allmendinger, R. W. (1998). Inverse and forward numerical modeling of trishear fault-propagation folds. Tectonics, 17(4), 640–656. https://doi.org/10.1029/98TC01907

Allmendinger, R. W. & Shaw, J. H. (2000). Estimation of fault propagation distance from fold shape: Implications for earthquake hazard assessment. Geology, 28(12), 1099–1102.

Cristallini, E. O. & Allmendinger, R. W. (2002). Backlimb trishear: a kinematic model for curved folds developed over angular fault bends. Journal of Structural Geology, 24(2), 289–295. https://doi.org/10.1016/S0191-8141(01)00063-3

Erslev, E. A. (1991). Trishear fault-propagation folding. Geology, 19, 617–620. https://doi.org/10.1130/0091-7613(1991)019<0617:TFPF>2.3.CO;2

Hardy, S. & Ford, M. (1997). Numerical modeling of trishear fault propagation folding. Tectonics, 16(5), 841–854. https://doi.org/10.1029/97TC01171

Zehnder, A. T. & Allmendinger, R. W. (2000). Velocity field for the trishear model. Journal of Structural Geology, 22, 1009–1014.